

# From Classification to Cross-Modal Understanding: Leveraging Vision-Language Models for Fine-Grained Renal Pathology

Zhenhao Guo<sup>1</sup>, Rachit Saluja<sup>2</sup>, Tianyuan Yao<sup>3</sup>, Quan Liu<sup>3</sup>, Junchao Zhu<sup>3</sup>, Haibo Wang<sup>4</sup>, Daniel Reisenbüchler<sup>5</sup>, Yuankai Huo<sup>3</sup>, Benjamin Liechty<sup>6</sup>, David J. Pisapia<sup>6</sup>, Kenji Ikemura<sup>6</sup>, Steven Salvatoree<sup>6</sup>, Surya Seshane<sup>6</sup>, Mert R. Sabuncu<sup>2,6</sup>, Yihe Yang<sup>6,7</sup>, Ruining Deng<sup>3,6</sup>

**1** New York University, New York, NY 10012, USA

**2** Cornell Tech, New York, NY 10044, USA

**3** Vanderbilt University, Nashville, TN, 37235, USA

**4** Carnegie Mellon University, Pittsburgh, PA 15213, USA

**5** University of Regensburg, Regensburg, Bavaria 93053, DE

**6** Weill Cornell Medicine, New York, NY 10065, USA

**7** Northwell Health, New Hyde Park, NY 11040, USA

## Abstract

Fine-grained glomerular subtyping is central to kidney biopsy interpretation, but clinically valuable labels are scarce and difficult to obtain. Existing computational pathology approaches instead tend to evaluate coarse diseased classification under full supervision with image-only models, so it remains unclear how vision-language models (VLMs) should be adapted for clinically meaningful subtyping under data constraints. In this work, we model fine-grained glomerular subtyping as a clinically realistic few-shot problem and systematically evaluate both pathology-specialized and general-purpose vision-language models under this setting. We assess not only classification performance (accuracy, AUC, F1) but also the geometry of the learned representations, examining feature alignment between image and text embeddings and the separability of glomerular subtypes. By jointly analyzing shot count, model architecture and domain knowledge, and adaptation strategy, this study provides guidance for future model selection and training under real clinical data constraints. Our results indicate that pathology-specialized vision-language backbones, when paired with the vanilla fine-tuning, are the most effective starting point. Even with only 4–8 labeled examples per glomeruli subtype, these models begin to capture distinctions and show substantial gains in discrimination and calibration, though additional supervision continues to yield incremental improvements. We also find that the discrimination between positive and negative examples is as important as image-text alignment. Overall, our results show that supervision level and adaptation strategy jointly shape both diagnostic performance and multimodal structure, providing guidance for model selection, adaptation strategies, and annotation investment.

## Keywords

Vision-Language Model, Fine-Grained Classification, Fine-tuning, Few-shot Learning, Digital Renal Pathology

## Article informations

©YYYY Name1 and Name2. License: CC-BY 4.0

Corresponding author: rud4004@med.cornell.edu

## 1. Introduction

**R**enal *histopathology* is central to diagnosis, subtyping, and prognosis in kidney disease Feng and Liu (2023); Sethi and Fervenza (2019); Schnuelle (2023); Wilson and Messias (2022). Fine-grained glomerular subtypes carry therapeutic and risk-stratification implications beyond coarse lesion detection of the International et al. (2009); Rafieian-Kopaei et al. (2013); Chen et al. (2022); Lu et al. (2025); Deng et al. (2022); Yu et al. (2025). Yet high-quality labels are expensive, inter-expert agreement

is limited, and cross-institution variation in staining and scanners induces domain shift Duenweg et al. (2023). In nephrectomy cohorts of renal cell carcinoma (RCC), surgical clamping of the renal artery, veins, or ureter produces ischemic artifacts such as glomerular basement membrane (GBM) wrinkling and capsular distention, so many glomeruli share similar ischemic-appearing changes. RCC patients also share common risk factors with diabetes, hypertension, and metabolic syndrome, and many glomeruli lie along a continuum from ischemia to segmental and then global sclerosis, often showing GBM wrinkling, multilayering of

Bowman's capsule, and tuft–capsule adhesions in the same glomerulus. These surgical and clinical factors blur the boundaries between ischemic, segmentally sclerotic, and globally sclerotic glomeruli, making it difficult for algorithms to distinguish between these groups. In practice, small labeled cohorts are the norm, and clinicians often reason with a few confirmed exemplars as references Crowley et al. (2003). Recent advances in foundation and vision–language models (VLMs) have transformed computational pathology, offering generalizable representations that bridge visual and textual modalities Cui et al. (2022); Chanda et al. (2024); Bilal et al. (2025); Ochi et al. (2025). However, standardized evidence for their fine-grained adaptation remains limited, complicating principled selection across backbones and parameter-efficient fine-tuning strategies. Prior studies typically evaluate only a single task granularity Campanella et al. (2019), supervision regime Lu et al. (2021), or adaptation strategy at a time Yao et al. (2022), often focusing on coarse normal-vs-diseased discrimination Wang et al. (2025), training under full supervision Yu et al. (2025), or image-only classification with one backbone and one split Yao et al. (2022), and rarely characterizing how performance scales with sample size Taher et al. (2025); Hosseinzadeh Taher et al. (2021). At the same time, the degree to which visual and textual features are aligned is increasingly viewed as central to the robustness and clinical reliability of VLMs in pathology Chen et al. (2024); Li and Tang (2024); Hanna et al. (2025). We address these gaps by (i) establishing a framework for fine-grained glomerular subtyping, (ii) characterizing model performance in a clinically realistic few-shot regime, and (iii) analyzing multimodal image-text feature-based alignment analysis. We evaluate both general-purpose and pathology-specialized backbones across prevailing architectures and multiple parameter-efficient adaptation strategies across few-shot settings using Monte Carlo resampling. Beyond measuring performance with classification metrics, we perform a cross-modal embedding analysis: we quantify image-text feature alignment and between-class separability as a function of supervision level, task granularity, and adaptation strategy. We then relate these representational properties to model performance and confidence. Taken together, this reveals how supervision and adaptation jointly shape multimodal alignment and downstream behavior, providing practical guidance for model selection under realistic data constraints.

Our contribution is threefold:

1. To our knowledge, we establish the first VLM benchmark for fine-grained glomerular subtyping in renal pathology, targeting pathologically actionable distinctions beyond coarse disease classification.
2. We characterize model behavior under realistic data limitations by restricting supervision to a few labeled exem-

plars per class and analyzing how backbone, parameter-efficient adaptation, and sample size jointly affect performance in general-purpose and pathology-specialized foundation models.

3. We introduce embedding-space analyses that quantify multimodal image-text feature alignment and between-class separability, and we show that these metrics track downstream accuracy and confidence, revealing trends that inform future cross-modal learning under few-shot constraints.

## 2. Related Works

### 2.1 Few-shot learning for medical image classification

Renal pathologists have established morphology-based systems for fine-grained glomerular classification. Recent work has further refined outcome assessment in focal segmental glomerulosclerosis through a new index Tervaert et al. (2010); Bajema et al. (2018); Chan et al. (2024). Together, these expert-defined schemas provide fine-grained and clinically meaningful labels that now serve as reliable ground truth for training AI models. However, pathology data are inherently scarce, costly to annotate, and highly heterogeneous across institutions and imaging protocols Madabhushi and Lee (2016); Shi et al. (2019); Li et al. (2025a). As a result, few-shot learning naturally emerges as a practical and clinically aligned approach that maintains robust performance with only a handful of examples per class. Prior studies indicate that such methods can substantially mitigate data scarcity and even approach fully supervised accuracy with very limited samples Pachetti and Colantonio (2024); Shakeri et al. (2022). Accordingly, few-shot learning provides a compelling direction for developing reliable and data-efficient pathology AI systems under low-annotation constraints.

### 2.2 Fine-grained Glomerular Classification

In recent years, deep learning and VLMs have achieved substantive progress in fine-grained glomerular classification. Deep learning, grounded in morphological patterns, has produced end to end convolutional pipelines on whole-slide images that cover glomerulus detection, disease categorization, and key lesion identification Yao et al. (2022); Lu et al. (2021); Yu et al. (2025); Weis et al. (2022); Lei et al. (2024); Li et al. (2025b). At the same time, the feasibility of VLMs for pathology classification has been increasingly demonstrated. They have shown strong performance Zheng et al. (2025); Guo et al. (2025b). Taken together, these studies provide converging evidence that both deep learning and VLMs are feasible for fine-grained glomerular classification.

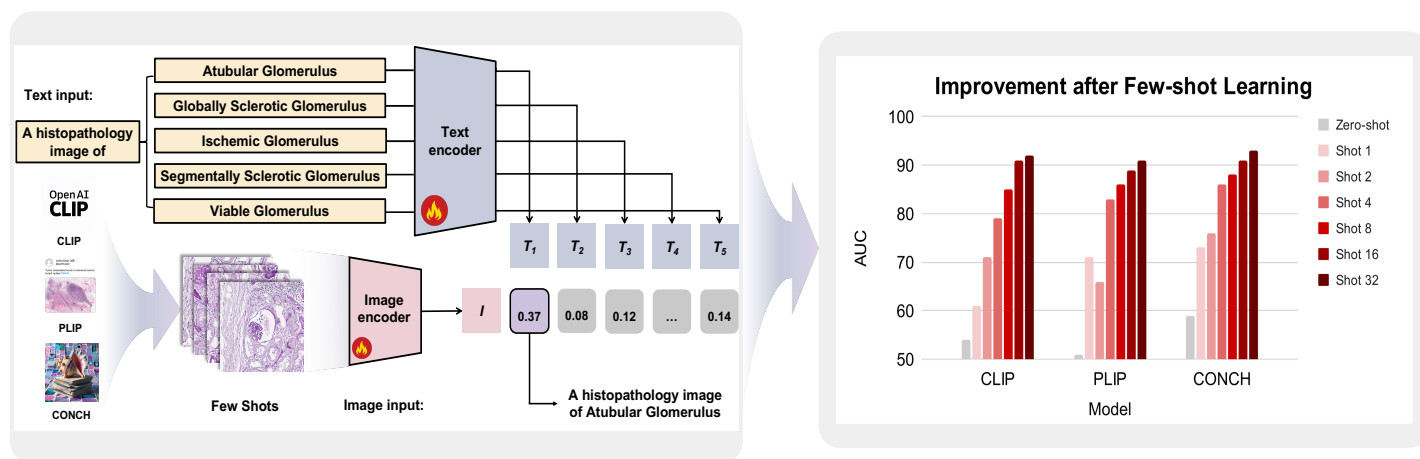


Figure 1: **Pipeline overview.** We train the image encoder and the text encoder in a few-shot setting, where only a small number of labels are provided for each glomerular subtype. For each shot, patches and their class descriptions are encoded, and the model is updated. As the number of shots increases, the performance improves.

### 2.3 Cross-modal Vision Language Models on Renal Pathology

In clinical practice, physicians engage in a multimodal and integrative diagnostic process, synthesizing information from diverse sources. This cross-modal verification ensures that diagnostic reasoning is both reliable and interpretable Roth et al. (2021); Cui et al. (2024); Jin et al. (2025). Analogously, to endow artificial intelligence systems with comparable credibility in medical contexts, it is essential to move beyond unimodal classification paradigms and promote modality alignment. Such alignment enables the model to ground its predictions in coherent morphological and textual evidence, thereby enhancing transparency and interpretability Kline et al. (2022); Simon et al. (2025). Moreover, effective modality alignment contributes to improved empirical performance, as it facilitates the extraction of stable and domain-general representations within a unified semantic space Wang and Isola (2020); Xu et al. (2024).

## 3. Methods

### 3.1 Pipeline Overview

To overcome the limited generalizability of existing methods for fine-grained pathological image classification, our approach centers on distinguishing among subtypes of diseased glomeruli within a low-data setting. Specifically, we investigate the adaptation of VLMs to a five-class glomerular pathology classification task, relying on only a small number of labeled examples per category. As depicted in Figure 1, the pipeline begins with pathological image patches paired with their corresponding class prompts (for example, “A histopathology image of Atubular Glomeru-

lus”). Both the images and textual prompts are encoded using a pretrained VLMs backbone, which is adapted to the task either through fine-tuning or the integration of lightweight modules. To reflect the low-data scenario, this adaptation is performed under few-shot conditions, where only a limited set of labeled exemplars per class is available to guide the alignment between modalities. This process yields high-dimensional embeddings for both images and prompts. To generate predictions, we compute the cosine similarity between each image embedding and all class prompt embeddings, applying a softmax transformation to produce a probability distribution over the classes. The model then assigns each image to the class with the highest similarity score.

### 3.2 Foundation VLMs Backbones

To systematically assess the influence of model design, domain expertise, and modality alignment, we select three VLM backbones, as illustrated in Figure 2 parts a and b, that differ in scale, architecture, and the extent of pathology-specific training. These are: a general-purpose foundation model (CLIP), a pathology-adapted CLIP model (PLIP), and a pathology-native foundation model (CONCH).

- CLIP:** A large-scale VLMs Radford et al. (2021), trained on roughly 400M images with natural language captions using a symmetric contrastive learning objective. In this work, we adopt the openai/clip-vit-base-patch16 variant, which employs a ViT-B/16 image encoder and a Transformer-based text encoder Dosovitskiy et al. (2020). Both encoders project their respective inputs into a shared embedding space, normalized for cosine similarity. CLIP enables zero-shot classification and retrieval by comparing the embeddings of images against those of natural

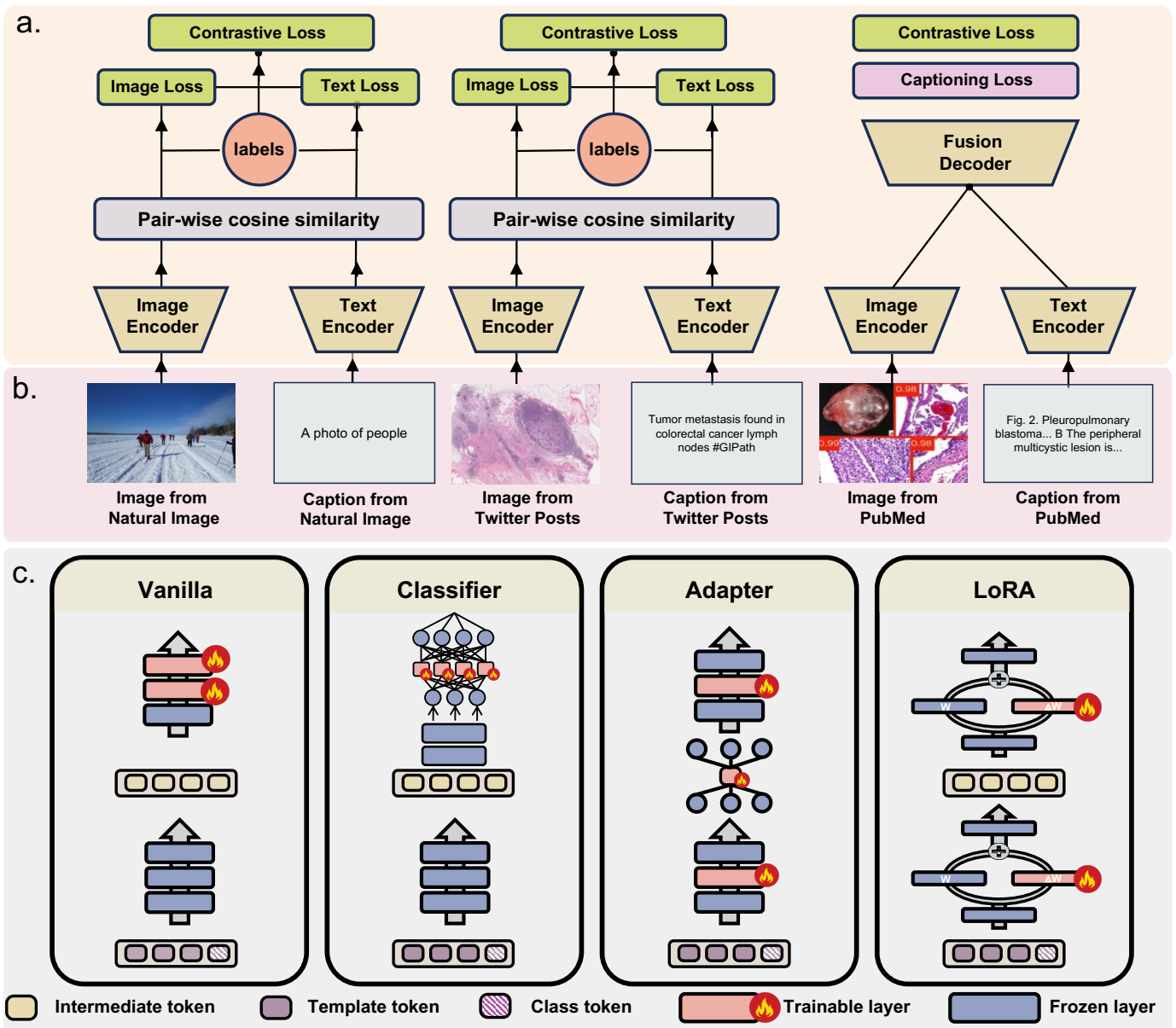


Figure 2: **(a) Model architectures.** We compare contrastive vision-language models with separate image and text encoders trained via pairwise cosine similarity, and a CoCa-style architecture with an additional fusion/decoder branch. **(b) Domain-specific training data.** We illustrate three sources of paired image-text data: natural images with generic captions, social media posts from Twitter with informal expert commentary, and biomedical figures from PubMed with pathology-style captions. **(c) Fine-tuning strategies.** We consider (i) vanilla fine-tuning, where all model parameters are updated; (ii) LoRA, which inserts low-rank trainable updates into frozen weight matrices; (iii) adapter tuning, which adds small trainable adapter modules between frozen layers; and (iv) classifier tuning, which keeps the backbone frozen and only trains a classifier head.

language prompts for similarity-based matching.

- **PLIP:** A pathology-adapted VLMs Huang et al. (2023), developed by retraining CLIP on over 200K pathology image-caption pairs collected primarily from Twitter posts. The model retains the dual-encoder architecture of CLIP, with a ViT-B/16 image encoder and a Transformer-based text encoder, and projects both modalities into a shared

embedding space. By aligning histopathology images with domain-specific textual descriptions, PLIP produces embeddings that are more sensitive to pathology-specific features and supports zero-shot classification and cross-modal retrieval in the medical imaging domain.

- **CONCH:** A pathology-native vision-language foundation model Lu et al. (2024), developed on the CoCa archi-

ture Yu et al. (2022) with a ViT-B/16 backbone. It is pretrained on 1.17M pathology image–caption pairs curated from PubMed and related pathology resources, combining contrastive alignment and caption generation objectives. By integrating structured attention pooling and a fusion decoder within the CoCa framework, CONCH learns fine-grained multimodal representations of high-resolution histology and supports zero-shot classification and cross-modal retrieval in the pathology domain.

### 3.3 Fine-tuning Strategies

To adapt VLMs for fine-grained glomerular classification in few-shot settings, we examine four fine-tuning approaches, as illustrated in Figure 2 part c, spanning full-parameter updates to highly parameter-efficient methods Gao et al. (2024); Srinivasan et al. (2024); Hu et al. (2022); Ioffe and Szegedy (2015). Vanilla fine-tuning modifies both image and text encoders, while Adapter and LoRA insert lightweight modules into the encoder to adjust internal representations with minimal disruption. Classifier tuning updates only the prediction head, keeping the backbone fixed. All methods use a supervised contrastive objective, computing class probabilities via cosine similarity between image and text embeddings followed by softmax.

- **Vanilla Fine-tuning Srinivasan et al. (2024):** This method unfreezes the top layers of the image and text encoders and jointly updates their parameters along with the task-specific head. By training these layers end-to-end, the model adjusts its high-level representations directly to the target task. However, this flexibility comes at the cost of higher computational demands.
- **Low-Rank Adaptation (LoRA) Hu et al. (2022):** This method injects additional trainable low-rank decomposition matrices into the attention projection layers of the top transformer blocks in both the vision and text encoders. During training, only low-rank decomposition matrices are updated while the original backbone weights remain frozen. The rank  $r$  controls the dimensionality of the adaptation subspace, and the scaling factor  $\alpha$  regulates the contribution of  $\Delta W$  to the final projection. This design reduces the number of trainable parameters while preserving the pretrained backbone.
- **Adapter Tuning Gao et al. (2024):** This approach preserves all pretrained encoder weights and introduces lightweight bottleneck adapter modules into the Transformer layers Pfeiffer et al. (2020). In our setup, we adopt *sequential bottleneck adapter*, which place a single adapter block only after the feed-forward network of each Transformer layer. Each adapter consists of a down-projection from the hidden dimension  $d$  to a smaller

bottleneck dimension  $m$ , a non-linear activation, and an up-projection back to  $d$ . The transformed output is then added to the residual stream. During training, only the adapter parameters are updated while the backbone remains frozen, enabling parameter-efficient adaptation with minimal additional overhead.

- **Classifier Tuning Ioffe and Szegedy (2015):** This method freezes all backbone parameters and trains only a lightweight classification head on top of the extracted image features. We evaluate three variants: (i) a single linear projection from the feature dimension to the number of classes; (ii) a two-layer multilayer perceptron (MLP) with a hidden layer and non-linear activation Guo et al. (2025a); and (iii) the same two-layer MLP augmented with batch normalization Ioffe and Szegedy (2015) applied after the hidden layer. In all cases, the classifier outputs class logits which are passed through a softmax for prediction. In our experiments, variant (iii) performs best, and we use it for all reported results.

## 4. Experiments and Data

### 4.1 Data

This study retrospectively analyzed the non-tumoral kidney parenchyma of eight radical nephrectomy cases processed at the Department of Pathology, Northwell Health, with specimens sourced from both Long Island Jewish Medical Center and Northshore University Hospital between July 2017 and October 2019.

### 4.2 Data Preprocessing

To standardize the model inputs, we begin by extracting image patches from the high-resolution WSIs. Individual glomeruli are first located using the provided annotation masks. For each identified glomerulus, we define a bounding box that is symmetrically expanded by 50 pixels on all sides to capture critical surrounding context. To ensure uniformity across samples, each bounding box is then reshaped to a square, yielding patches with consistent input dimensions.

For the textual component, we generate class-specific prompts that serve as anchors for contrastive learning. Each of the five glomerular subtypes is represented by a standardized phrase in the form: “A histopathology image of {label}.” The text prompt is kept fixed in all experiments for consistency in image-text alignment.

To ensure valid few-shot evaluation, we build class-balanced training sets with 1, 2, 4, 8, 16, and 32 shots per class. We enforce strict WSI-level separation. All training patches come only from training WSIs. The validation set uses only WSIs that never appear in training. For

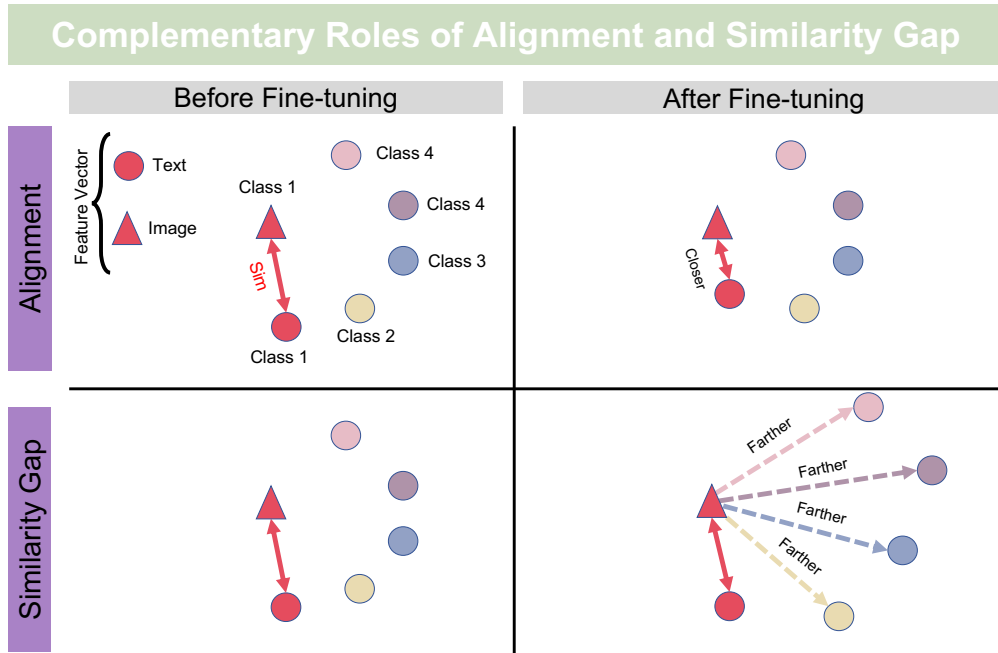


Figure 3: **Complementary roles of alignment and similarity gap.** It shows the change in image and text feature vectors before and after fine-tuning. Alignment measures whether fine-tuning pulls an image embedding closer to the embedding of its own positive text description. The similarity gap measures whether fine-tuning pushes an image embedding farther away from text embeddings of other (negative) classes. Together, these two effects capture how fine-tuning reduces within-class image-text distance while enlarging across-class distance.

each run and class, we first form a 32-sample superset from the training WSIs. We fix a per-run permutation and derive smaller shots as prefixes of this order, where each smaller-shot subset is fully contained within all larger-shot sets. This design guarantees that, for example, the 4-shot configuration contains the exact images from the 2-shot set plus two additional images per class, enabling a controlled comparison across shot levels. We also maximize diversity across runs, especially for small shots. Each run receives a distinct round robin slice of the per-class pool, and we prioritize that slice to reduce overlap across runs. All sampling uses fixed random seeds and deterministic rules.

### 4.3 Experimental Design

To ensure robust and stable model optimization, we performed a systematic exploration of key hyperparameters. Training was conducted using the Adam optimizer, incorporating a linear warm-up stage followed by a scheduled decay to promote smooth and consistent convergence. To further strengthen generalization and mitigate overfitting, we uniformly applied data augmentation techniques implemented via the Albumentations Buslaev et al. (2020) library and employed early stopping with consistent patience and minimum delta parameters across all experiments. All experiments were conducted on an NVIDIA RTX 6000 Ada Generation with 48 GB of VRAM. For quantitative results,

we report the mean and standard deviation over 10 independent runs. UMAP visualizations are generated from the run achieving the highest AUC.

### 4.4 Evaluation Metrics

We evaluated all methods on a five-class glomerular classification task using a fixed train-validation split and standardized class prompts. Performance was reported using overall accuracy, macro-AUC, and F1 score, with identical data augmentation and early stopping applied to ensure a fair comparison.

In addition to standard metrics, we further assessed internal representation alignment by measuring the alignment and similarity gap, as depicted in Figure 3. Alignment quantifies the average cosine similarity between paired image-text embeddings, reflecting how well the two modalities are semantically matched, and is computed as:

$$\text{Alignment} = \frac{1}{N} \sum_{i=1}^N \cos(\mathbf{z}_i, \mathbf{w}_{y_i}) = \frac{1}{N} \sum_{i=1}^N \frac{\mathbf{z}_i^\top \mathbf{w}_{y_i}}{\|\mathbf{z}_i\|_2 \|\mathbf{w}_{y_i}\|_2}. \quad (1)$$

The similarity gap measures the mean separation between positive and negative pairs, capturing the model’s discriminative ability in distinguishing aligned from unaligned representations and is defined as:

## ROC Comparison of Backbones and Fine-tuning Strategies Across Shots

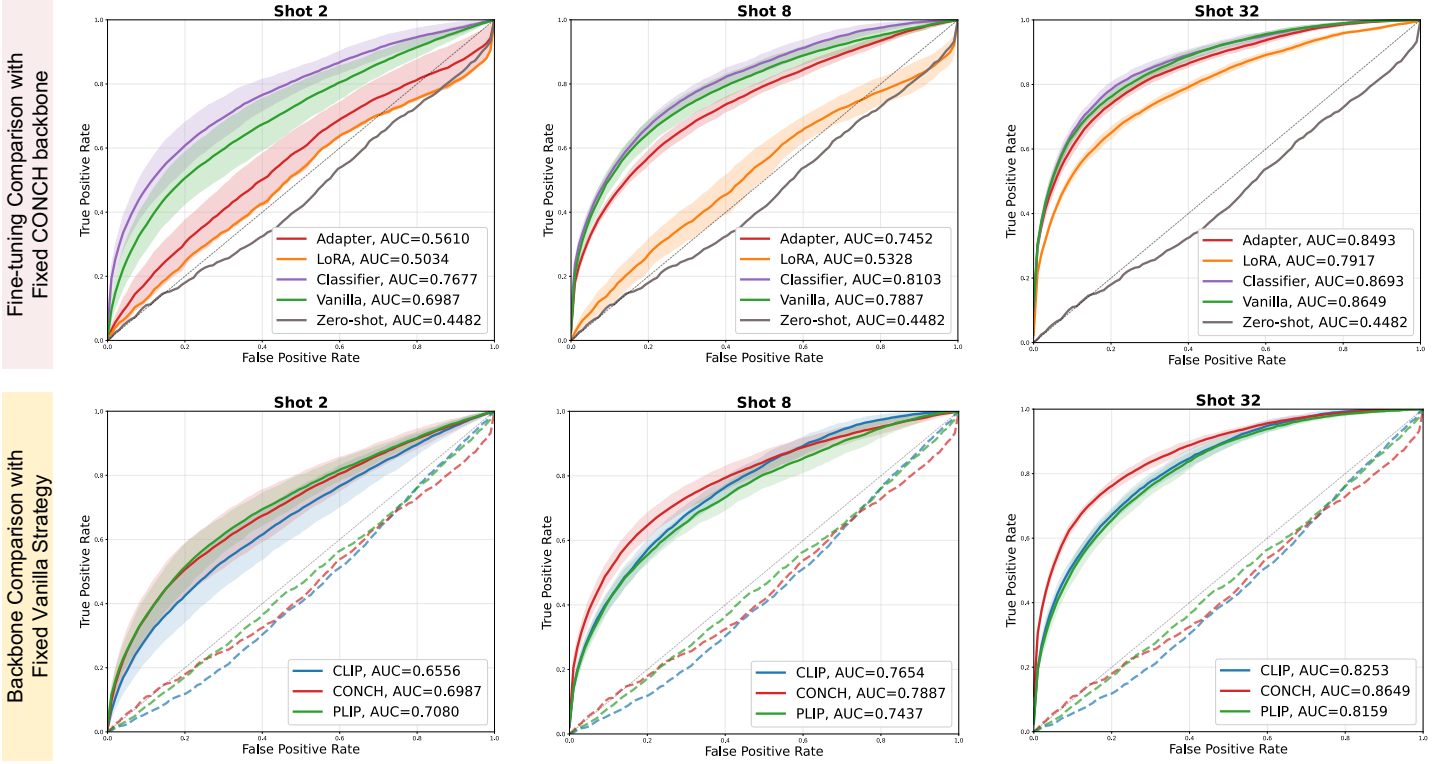


Figure 4: **ROC curves across models and fine-tuning methods as shot counts increase.** We compare two axes, model comparison (fixed strategy) and fine-tuning method comparison (fixed backbone), by plotting true positive rate (TPR) versus false positive rate (FPR) across increasing shot counts.

$$\text{Similarity Gap} = \frac{\overbrace{\frac{1}{N} \sum_{i=1}^N \cos(\mathbf{z}_i, \mathbf{w}_{y_i})}^{\text{mean positive similarity}}}{\underbrace{\frac{1}{N(N-1)} \sum_{i \neq j} \cos(\mathbf{z}_i, \mathbf{w}_{y_j})}_{\text{mean negative similarity}}} \quad (2)$$

where  $\mathbf{z}_i$  and  $\mathbf{w}_{y_i}$  denote the normalized text and image embeddings of the  $i$ -th sample, respectively. Together, these two metrics provide complementary perspectives on multimodal consistency. We also visualized multimodal feature distributions using UMAP for dimensionality reduction and kernel density estimation (KDE) for density-based visualization to provide qualitative insights. UMAP was chosen as it provides a compact yet faithful two-dimensional representation of the embedding space, facilitating visual comparison of inter-class and cross-modal distributions. All UMAP embeddings and KDE visualizations were produced using consistent settings across experiments.

Beyond alignment-based measures, we report Intra Class Distance and Silhouette Score. For intra class distance, let  $\mathbf{x}_i \in \mathbb{R}^{512}$  be the original image embedding and  $y_i$  its class

label. We obtain the two-dimensional UMAP projection  $\mathbf{u}_i = \text{UMAP}(\mathbf{x}_i)$  using fixed hyperparameters and seed across experiments. Intra class distance is the mean pairwise euclidean distance among same-class samples in the UMAP space:

$$d_{\text{Euc}}(\mathbf{a}, \mathbf{b}) = \|\mathbf{a} - \mathbf{b}\|_2, \\ \text{ICD} = \frac{1}{|\mathcal{C}|} \sum_{c \in \mathcal{C}} \frac{2}{n_c(n_c - 1)} \sum_{\substack{i < j \\ y_i = y_j = c}} d_{\text{Euc}}(\mathbf{u}_i, \mathbf{u}_j). \quad (3)$$

where  $\mathcal{C}$  is the set of classes and  $n_c$  is the number of samples in class  $c$ . To assess separability in the original feature space, we compute the Silhouette score on  $\{\mathbf{x}_i\}$  with cosine distance:

$$a_i = \frac{1}{n_{y_i} - 1} \sum_{\substack{j \neq i \\ y_j = y_i}} d_{\cos}(\mathbf{x}_i, \mathbf{x}_j), \\ b_i = \min_{k \neq y_i} \frac{1}{n_k} \sum_{y_j = k} d_{\cos}(\mathbf{x}_i, \mathbf{x}_j), \quad (4) \\ s_i = \frac{b_i - a_i}{\max\{a_i, b_i\}}, \quad S = \frac{1}{N} \sum_{i=1}^N s_i.$$

Model	Method	Accuracy						
		0	1	2	4	8	16	32
ResNet	Supervised learning He et al. (2016)	0.0000±0.0000	0.2003±0.0026	0.1005±0.0005	0.1645±0.0037	0.2281±0.0898	0.2993±0.1284	0.2208±0.0649
CLIP	Classifier Ioffe and Szegedy (2015)	0.3050±0.0000	<b>0.3898</b> ±0.2092	0.2381±0.1725	0.3476±0.1963	0.3153±0.1893	0.2498±0.2086	0.4499±0.0798
	LoRA Hu et al. (2022)	0.3050±0.0000	0.3591±0.0513	0.4325±0.0948	0.4367±0.0603	0.4916±0.0773	0.5581±0.0767	0.6232±0.1033
	Adapter Gao et al. (2024)	0.3050±0.0000	0.2581±0.1140	0.3566±0.0984	0.4367±0.0784	0.4823±0.0698	0.5242±0.0636	0.5809±0.0475
	Vanilla Srinivasan et al. (2024)	0.3050±0.0000	0.3347±0.1020	0.4359±0.1380	0.5114±0.0914	0.5715±0.0609	0.5998±0.0604	0.6331±0.0666
CONCH	Classifier Ioffe and Szegedy (2015)	0.0512±0.0000	0.3181±0.1146	0.4346±0.2026	0.4579±0.1704	0.4318±0.1930	0.6235±0.1357	0.6581±0.1772
	LoRA Hu et al. (2022)	0.0512±0.0000	0.0512±0.0001	0.0510±0.0001	0.0544±0.0049	0.1119±0.0996	0.5150±0.0226	0.6565±0.0262
	Adapter Gao et al. (2024)	0.0512±0.0000	0.0512±0.0000	0.1643±0.1339	0.1974±0.2253	0.5987±0.0401	0.6824±0.0389	0.7610±0.0276
	Vanilla Srinivasan et al. (2024)	0.0512±0.0000	0.3744±0.1583	0.4449±0.1695	0.5029±0.0709	<b>0.6058</b> ±0.0953	<b>0.6862</b> ±0.0813	<b>0.7837</b> ±0.0186
PLIP	Classifier Ioffe and Szegedy (2015)	<b>0.3173</b> ±0.0000	0.2971±0.1953	0.2704±0.2702	0.2482±0.1782	0.3439±0.2007	0.2864±0.1409	0.3074±0.1032
	LoRA Hu et al. (2022)	<b>0.3173</b> ±0.0000	0.2203±0.1158	0.2356±0.0884	0.2496±0.0373	0.4540±0.0767	0.5408±0.0646	0.5972±0.0513
	Adapter Gao et al. (2024)	<b>0.3173</b> ±0.0000	0.3740±0.1264	0.4856±0.0744	0.5297±0.0478	0.5132±0.0458	0.5617±0.0421	0.5776±0.0313
	Vanilla Srinivasan et al. (2024)	<b>0.3173</b> ±0.0000	0.3793±0.1005	<b>0.5361</b> ±0.0730	<b>0.5745</b> ±0.0548	0.5746±0.0678	0.5788±0.0264	0.5895±0.0443

Model	Method	AUC						
		0	1	2	4	8	16	32
ResNet	Supervised learning He et al. (2016)	0.0000±0.0000	0.4861±0.0006	0.4822±0.0003	0.5321±0.0017	0.4847±0.0537	0.5124±0.0388	0.5515±0.0611
CLIP	Classifier Ioffe and Szegedy (2015)	0.4368±0.0000	0.6150±0.0784	0.6589±0.0377	0.6952±0.0276	0.7128±0.0332	0.7171±0.0274	0.7552±0.0330
	LoRA Hu et al. (2022)	0.4368±0.0000	0.5705±0.0503	0.6132±0.0433	0.6377±0.0212	0.7220±0.0142	0.7647±0.0189	0.8057±0.0164
	Adapter Gao et al. (2024)	0.4368±0.0000	0.5799±0.0525	0.5910±0.0457	0.6189±0.0237	0.6854±0.0231	0.7366±0.0246	0.7635±0.0177
	Vanilla Srinivasan et al. (2024)	0.4368±0.0000	0.6108±0.0548	0.6556±0.0532	0.7091±0.0369	0.7654±0.0209	0.7896±0.0204	0.8253±0.0155
CONCH	Classifier Ioffe and Szegedy (2015)	0.4482±0.0000	<b>0.7401</b> ±0.0430	<b>0.7677</b> ±0.0301	<b>0.8108</b> ±0.0301	<b>0.8103</b> ±0.0144	<b>0.8459</b> ±0.0131	<b>0.8693</b> ±0.0114
	LoRA Hu et al. (2022)	0.4482±0.0000	0.5034±0.0006	0.5034±0.0014	0.5114±0.0124	0.5328±0.0480	0.7241±0.0044	0.7917±0.0071
	Adapter Gao et al. (2024)	0.4482±0.0000	0.5035±0.0001	0.5610±0.0606	0.5659±0.0955	0.7452±0.0139	0.7956±0.0144	0.8493±0.0093
	Vanilla Srinivasan et al. (2024)	0.4482±0.0000	0.6368±0.0615	0.6987±0.0523	0.7480±0.0363	0.7887±0.0243	0.8209±0.0164	0.8649±0.0083
PLIP	Classifier Ioffe and Szegedy (2015)	<b>0.4672</b> ±0.0000	0.6338±0.0368	0.6986±0.0513	0.7240±0.0336	0.7353±0.0240	0.7605±0.0287	0.7697±0.0226
	LoRA Hu et al. (2022)	<b>0.4672</b> ±0.0000	0.5922±0.0388	0.6270±0.0467	0.6460±0.0196	0.7043±0.0130	0.7476±0.0091	0.8195±0.0173
	Adapter Gao et al. (2024)	<b>0.4672</b> ±0.0000	0.6220±0.0560	0.6589±0.0315	0.6732±0.0196	0.7238±0.0157	0.7633±0.0133	0.7896±0.0107
	Vanilla Srinivasan et al. (2024)	<b>0.4672</b> ±0.0000	0.6557±0.0481	0.7080±0.0323	0.7296±0.0282	0.7437±0.0242	0.7856±0.0100	0.8159±0.0147

Model	Method	F1						
		0	1	2	4	8	16	32
ResNet	Supervised learning He et al. (2016)	0.0000±0.0000	0.1023±0.0012	0.0526±0.0011	0.1412±0.0021	0.1506±0.0457	0.1445±0.0205	0.1672±0.0360
CLIP	Classifier Ioffe and Szegedy (2015)	0.1049±0.0000	0.1534±0.0810	0.0875±0.0459	0.1031±0.0544	0.1033±0.0583	0.0753±0.0493	0.1378±0.0403
	LoRA Hu et al. (2022)	0.1049±0.0000	0.1833±0.0380	0.2441±0.0419	0.2618±0.0249	0.3244±0.0380	0.3849±0.0270	0.4198±0.0416
	Adapter Gao et al. (2024)	0.1049±0.0000	0.1770±0.0609	0.2249±0.0536	0.2658±0.0368	0.3030±0.0350	0.3437±0.0288	0.3808±0.0259
	Vanilla Srinivasan et al. (2024)	0.1049±0.0000	0.2348±0.0604	0.2849±0.0709	0.3418±0.0487	0.3797±0.0262	0.3955±0.0268	0.4254±0.0418
CONCH	Classifier Ioffe and Szegedy (2015)	0.0534±0.0000	0.1781±0.0558	0.2972±0.1072	0.3280±0.0932	0.3237±0.1043	0.4229±0.0646	0.4567±0.0811
	LoRA Hu et al. (2022)	0.0534±0.0000	0.0534±0.0004	0.0532±0.0006	0.0566±0.0051	0.0953±0.0678	0.3194±0.0137	0.4011±0.0135
	Adapter Gao et al. (2024)	0.0534±0.0000	0.0534±0.0000	0.1200±0.0761	0.1313±0.1212	0.3509±0.0208	0.3993±0.0220	0.4752±0.0165
	Vanilla Srinivasan et al. (2024)	0.0534±0.0000	0.2293±0.0818	0.2774±0.0826	0.3285±0.0484	<b>0.3907</b> ±0.0376	<b>0.4397</b> ±0.0333	<b>0.5038</b> ±0.0101
PLIP	Classifier Ioffe and Szegedy (2015)	<b>0.1404</b> ±0.0000	0.1136±0.0645	0.1205±0.1087	0.1050±0.0574	0.1394±0.0802	0.1038±0.0392	0.1053±0.0352
	LoRA Hu et al. (2022)	<b>0.1404</b> ±0.0000	0.1438±0.0602	0.1765±0.0472	0.1994±0.0195	0.3086±0.0226	0.3642±0.0182	0.4319±0.0257
	Adapter Gao et al. (2024)	<b>0.1404</b> ±0.0000	0.2400±0.0571	0.3023±0.0390	0.3092±0.0229	0.3399±0.0268	0.3919±0.0261	0.4033±0.0290
	Vanilla Srinivasan et al. (2024)	<b>0.1404</b> ±0.0000	<b>0.2584</b> ±0.0539	<b>0.3341</b> ±0.0319	<b>0.3527</b> ±0.0308	0.3667±0.0313	0.4034±0.0085	0.4241±0.0300

Table 1: **Few-shot performance on fine-grained classification.** Accuracy, AUC, and F1 scores (Mean±SD) for three vision-language backbones under four fine-tuning strategies across shots  $\{0, 1, 2, 4, 8, 16, 32\}$ , with ResNet as a traditional image-only baseline. “Shots” denotes the number of labeled images per class used for fine-tuning; 0 indicates no fine-tuning baseline.

$$S \in [-1, 1].$$

## 5. Results

### 5.1 Classification Performance

Table 1 and Figure 4 demonstrate a consistent improvement as supervision increases: accuracy, AUC, and F1 rise monotonically from 0 to 32 shots and begin to plateau around 8–16 shots. The earlier gains in AUC relative to accuracy/F1 indicate that models acquire ranking ability with very limited labels, while classification requires additional supervision. Consistently, combinations of pathology-specialized backbones with full-parameter fine-tuning or Adapter yield ROC

curves closest to the upper-left corner.

Across backbones, PLIP exhibits the smoothest and most stable progression, with steadily increasing AUC and F1 and minimal variance across shots. This pattern is consistent with strong initial alignment to pathology semantics and robust transfer under scarce labels. CONCH is less stable in the extreme low-shot regime, but once modest supervision is available, it accelerates rapidly and becomes competitive at higher shots. CLIP underperforms at the lowest shots yet benefits the most from additional labels, narrowing the gap by 16 to 32 shots.

Among adaptation strategies, vanilla fine-tuning yields the most persistent, cumulative improvements and



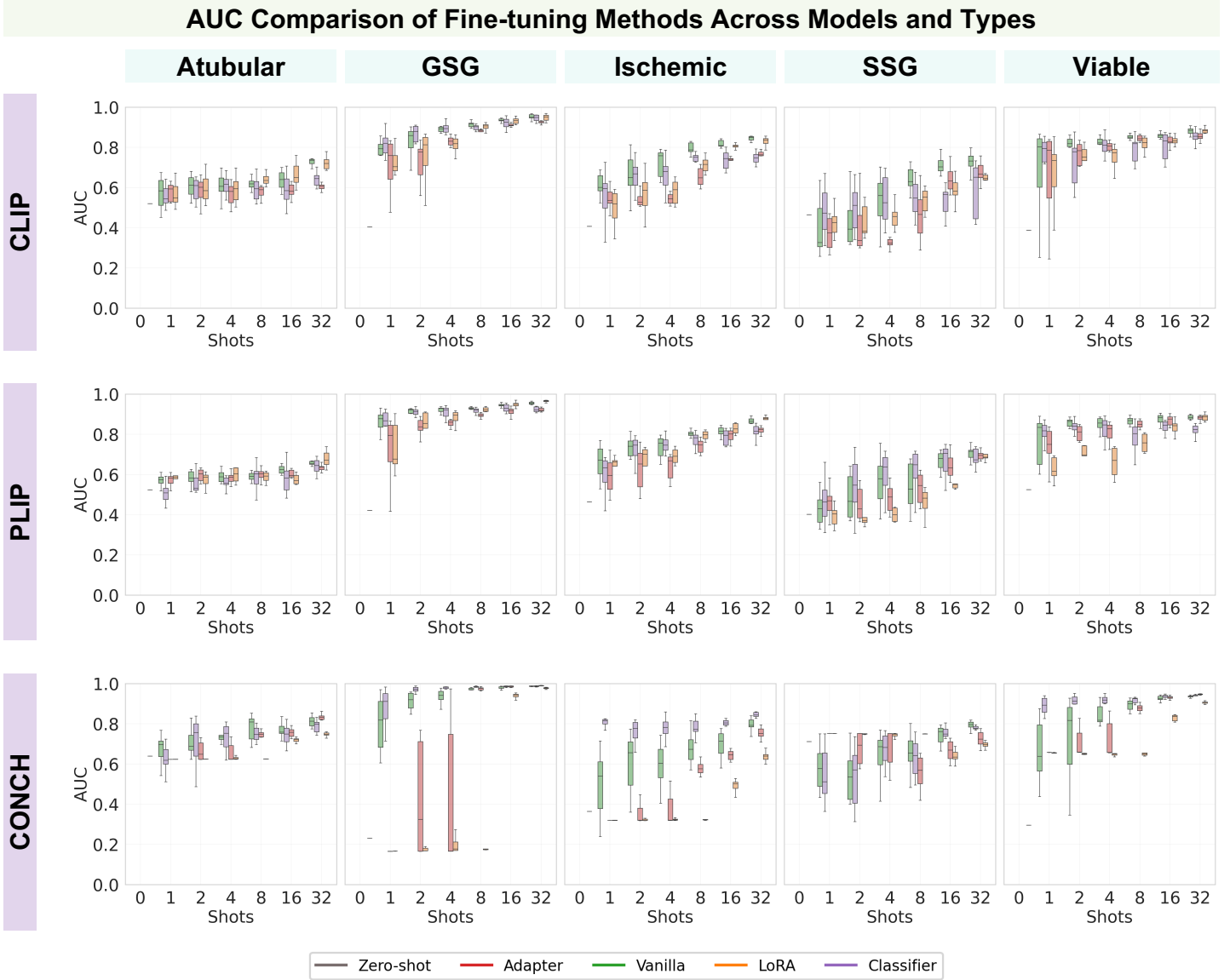


Figure 5: **Discrimination across subtypes.** This figure summarizes per-class discrimination performance across 10 runs. For each glomerular subtype, we report the distribution of AUC for different VLMs, fine-tuning strategies, and numbers of shots.

Model	Method	Intra Class Distance							Silhouette Score							
		Shots	0	1	2	4	8	16	32	0	1	2	4	8	16	32
CONCH Lu et al. (2024)	Classifier Ioffe and Szegedy (2015)		0.1827	0.1297	0.2644	0.3879	0.3819	0.2985	0.3983	0.1496	0.1566	0.1706	0.2190	0.1958	0.2037	0.2759
	LoRA Hu et al. (2022)		0.1827	0.1825	0.1792	0.1798	0.1816	0.1558	0.1406	0.1496	0.1495	0.1487	0.1490	0.1493	0.1470	0.1584
	Adapter Gao et al. (2024)		0.1827	0.1826	0.1521	0.1278	0.0948	0.0809	0.0802	0.1496	0.1496	0.1375	0.1407	0.1468	0.1862	0.2872
	Vanilla Srinivasan et al. (2024)		0.1827	0.1813	0.1820	0.1852	0.1868	0.1804	0.1644	0.1496	0.1480	0.1487	0.1516	0.1623	0.1635	0.1851

Table 2: Few-shot performance under the CONCH backbone across shots  $\{0, 1, 2, 4, 8, 16, 32\}$  for four fine-tuning strategies. Intra-Class Distance quantifies within-class compactness in the UMAP projection. Silhouette Score evaluates cluster separability in the original dimension using cosine distance

often achieves the highest accuracy/AUC under high-shot conditions. LoRA tuning remains moderate across all shots, while Adapter lags early but improves steadily with more data. Classifier tuning is more volatile: with CLIP/PLIP it may stagnate or regress at 1–4 shots, whereas with CONCH it performs strongly; conversely, when alignment is weak,

head-only updates cannot bridge the representational gap.

Qualitatively (Figure 5), PLIP exhibits the best overall behavior: its confidence distributions are the most stable and concentrated. Vanilla fine-tuning delivers the strongest overall performance, yielding the highest confidence medians with visibly compressed variance in most class distributions.

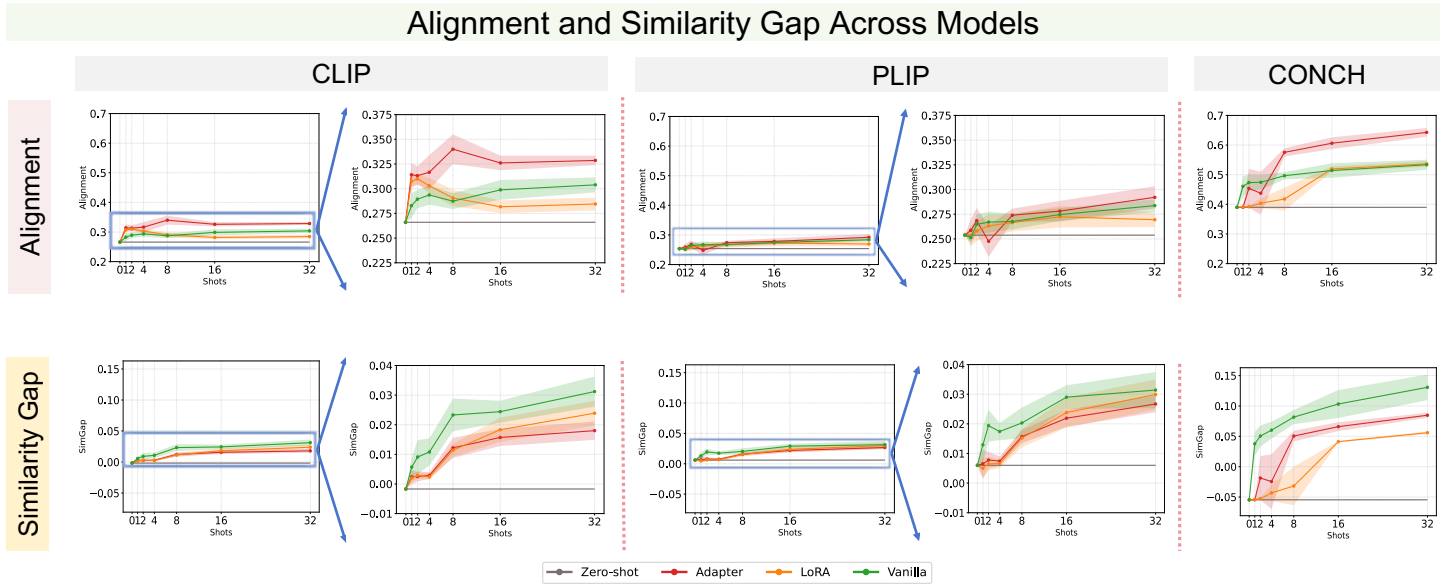


Figure 6: **Alignment and similarity gap across models.** This figure reports alignment and the similarity gap for different VLMs. CLIP and PLIP are demonstrated in both regular and enlarged panels to show their behavior.

By class difficulty, Atubular Glomerulus is the easiest to distinguish, showing higher medians and tighter boxplots with fewer outliers. Ischemic Glomerulus and Segmentally Sclerotic Glomerulus remain the most challenging, with broader spreads and longer whiskers across models and methods. Viable Glomerulus sits in between, with moderate medians and variance.

## 5.2 Cross-Multimodalities Comparison

As shown in Figures 6, 7 and table 2, we compare multiple backbones and fine-tuning methods across all shot settings, reporting Alignment and Similarity Gap. CONCH exhibits the most stable and pronounced gains as the number of shots increases. For cross-modal alignment, Adapter is consistently the top performer across backbones, whereas for the similarity-gap metric, Vanilla performs best. For all UMAP visualizations, we present results using CONCH as the representative example to illustrate the observed patterns. Adapter again achieves the best results in this setting, underscoring its strong cross-modal alignment capability. As shots increase, Intra-Class Distance in the UMAP space decreases for Adapter/LoRA/Vanilla but rises for the classifier-only head, whereas the Silhouette score in the original feature space increases across all methods, indicating stronger cluster separability. This upward Silhouette trend serves as a proxy for encoder quality, while Intra-Class Distance directly reflects whether same-class embeddings coalesce.

## 5.3 Discussion

As supervision increases from 0 to 32 shots, accuracy, AUC, and F1 rise. AUC improves earlier than accuracy and F1, indicating that ranking and score calibration emerge with very limited labels, whereas stable class assignment benefits from additional supervision. Backbone trajectories differ. PLIP progresses smoothly with low variance; CONCH is less stable at the very lowest shots but accelerates once modest supervision is available; CLIP underperforms in the extreme low-shot regime yet responds most strongly to additional labels, narrowing the gap by 16–32 shots. On the method axis, Vanilla tends to lead under higher-shot conditions; Adapter and LoRA lag initially but catch up around 16–32 shots; and Classifier-only tuning inherits the backbone’s initial alignment. When the backbone already provides a good global ordering, it achieves high AUC. However, with the backbone frozen, the classifier can only reweight existing features, preserving relative ranking but yielding biased boundaries and poor calibration, which lowers accuracy and F1.

Cross-modal analyses provide further insight. Although Adapter achieves the strongest alignment across backbones, its classification metrics remain moderate. In contrast, Vanilla attains the highest accuracy and F1, coinciding with larger similarity-gap values. This suggests that effective cross-modal representation requires not only pulling matched text–image pairs together but also sufficiently separating mismatched pairs.

At the lesion level, the per-class AUC trajectories (Figure 5) confirm that the ischemia, segmental sclerosis, and global sclerosis axis remains the most challenging for

## KDE and UMAP Visualization of the CONCH Model Under Various Fine-Tuning Methods and Shot Settings

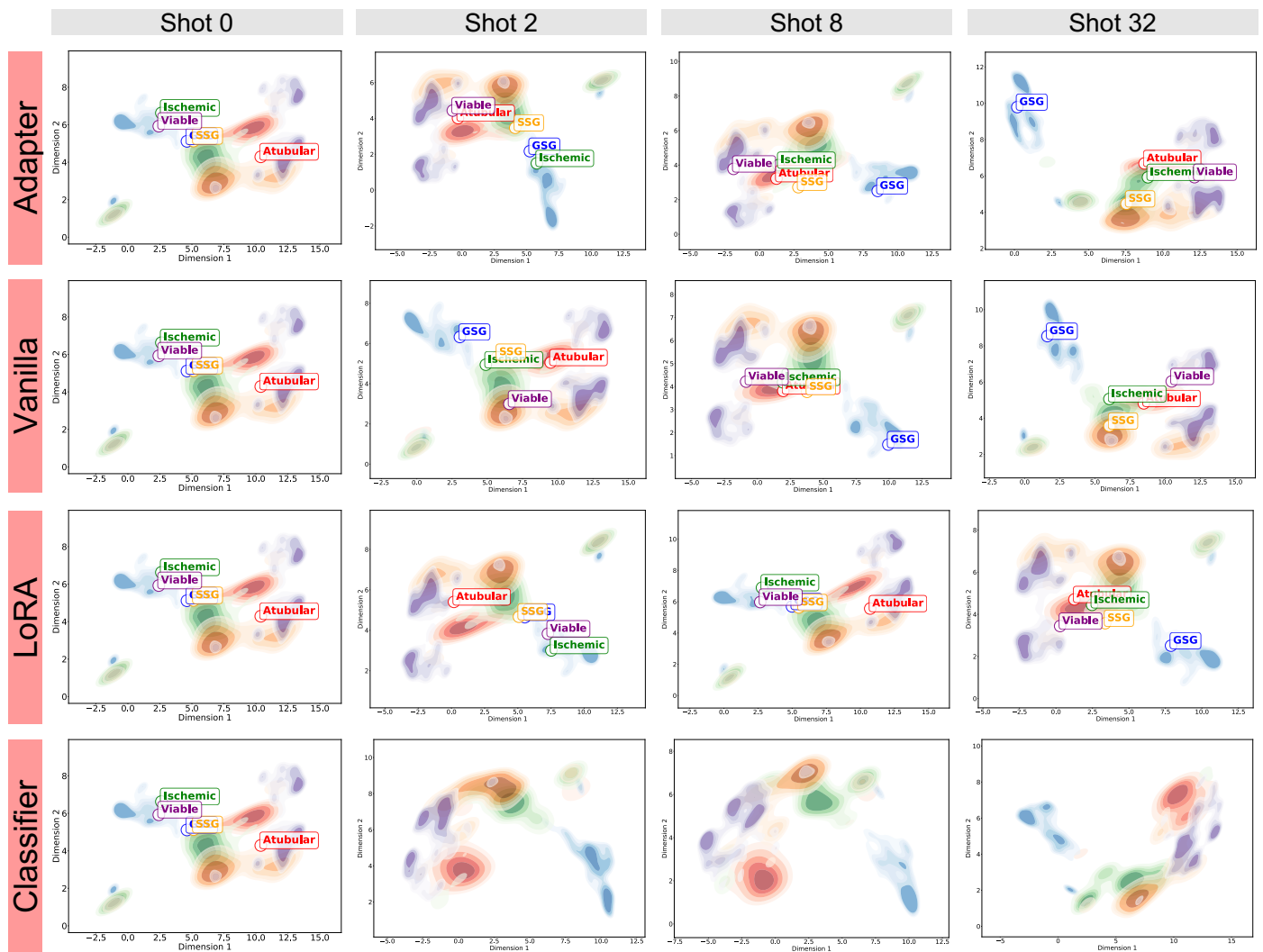


Figure 7: **UMAP/KDE visualization of embeddings across shots.** This plot shows text and image embeddings from the best CONCH run under different shot settings. For the classifier, which does not use text during adaptation, only image embeddings are shown. A companion table 2 reports Intra Class Distance and the standard Silhouette coefficient.

VLM-based models. This pattern mirrors the clinical continuum described. Our results therefore indicate that modern VLMs, while able to exploit limited supervision, still struggle to cleanly separate these closely related subtypes and inherit the morphologic ambiguity.

Taken together, these results indicate that pathology-specialized backbones such as CONCH, combined with Vanilla adaptation, can already extract useful signal with as few as 4–8 shots per class, and continue to improve as more supervision becomes available. At the same time, gains in multimodal alignment do not automatically translate to optimal classification unless the adaptation strategy can reshape both positive and negative pair structure. Overall, the interaction between supervision level and adaptation strategy determines both downstream performance and

multimodal behavior.

## 6. Conclusion

In this study, we frame fine-grained glomerular subtyping as a clinically realistic few-shot problem and use it to jointly examine supervision, adaptation strategy, and multimodal representation. We show that performance improves consistently with additional supervision, with meaningful gains already emerging from only a handful of labeled exemplars per class. Pathology-specialized vision–language backbones offer a clear advantage in the extreme low-shot regime, but this gap narrows as more supervision becomes available. We also find that adaptation strategy governs not only accuracy but also how image and text features are organized. These

observations indicate that multimodal alignment alone is not sufficient; how the model reshapes decision boundaries under limited labels is equally critical. Taken together, our results provide actionable guidance for selecting models and allocating annotation effort under data constraints, and they highlight alignment- and separability-based embedding metrics as interpretable indicators of clinical readiness.

## Acknowledgments

This research was supported by the WCM Radiology AIMI Fellowship and WCM CTSC 2026 Pilot Award. This research was also supported by NIH R01DK135597 and the KPMP Glue Grant.

## Ethical Standards

The work follows appropriate ethical standards in conducting research and writing the manuscript, following all applicable laws and regulations regarding treatment of animals or human subjects.

## Conflicts of Interest

We declare we don't have conflicts of interest.

## Data availability

In accordance with institutional regulations and in order to safeguard patient privacy and confidentiality, the datasets analyzed during this study cannot be shared and are not publicly available.

## References

- Ingeborg M Bajema, Suzanne Wilhelmus, Charles E Alpers, Jan A Bruijn, Robert B Colvin, H Terence Cook, Vivette D D'Agati, Franco Ferrario, Mark Haas, J Charles Jennette, et al. Revision of the international society of nephrology/renal pathology society classification for lupus nephritis: clarification of definitions, and modified national institutes of health activity and chronicity indices. *Kidney international*, 93(4):789–796, 2018.
- Mohsin Bilal, Manahil Raza, Youssef Altherwy, Anas Al-suhaibani, Abdulrahman Abduljabbar, Fahdah Almarshad, Paul Golding, Nasir Rajpoot, et al. Foundation models in computational pathology: A review of challenges, opportunities, and impact. *arXiv preprint arXiv:2502.08333*, 2025.
- Alexander Buslaev, Vladimir I. Iglovikov, Eugene Khvedchenya, Alex Parinov, Mikhail Druzhinin, and Alexandr A. Kalinin. Alumentations: Fast and flexible image augmentations. *Information*, 11(2), 2020. ISSN 2078-2489. URL <https://www.mdpi.com/2078-2489/11/2/125>.
- Gabriele Campanella, Matthew G Hanna, Luke Geneslaw, Allen Miraflor, Vitor Werneck Krauss Silva, Klaus J Busam, Edi Brogi, Victor E Reuter, David S Klimstra, and Thomas J Fuchs. Clinical-grade computational pathology using weakly supervised deep learning on whole slide images. *Nature medicine*, 25(8):1301–1309, 2019.
- Liu Chan, Yang Danyi, and Chao Chen. A new index for the outcome of focal segmental glomerulosclerosis. *Scientific Reports*, 14(1):8278, 2024.
- Dibaloke Chanda, Milan Aryal, Nasim Yahya Soltani, and Masoud Ganji. A new era in computational pathology: A survey on foundation and vision-language models. *arXiv preprint arXiv:2408.14496*, 2024.
- Qi Chen, Ruoshan Zhao, Sinuo Wang, Vu Minh Hieu Phan, Anton van den Hengel, Johan Verjans, Zhibin Liao, Minh-Son To, Yong Xia, Jian Chen, et al. A survey of medical vision-and-language applications and their techniques. *arXiv preprint arXiv:2411.12195*, 2024.
- Ying Chen, Yiya Yang, Yumei Liang, Manting Liu, Wei Xiao, and Xiaofang Hu. Retrospective analysis of crescent score in clinical prognosis of iga nephropathy. *Open Medicine*, 17(1):205–215, 2022.
- Rebecca S Crowley, Gregory J Naus, Jimmie Stewart III, and Charles P Friedman. Development of visual diagnostic expertise in pathology: an information-processing study. *Journal of the American Medical Informatics Association*, 10(1):39–51, 2003.
- Can Cui, Han Liu, Quan Liu, Ruining Deng, Zuhayr Asad, Yaohong Wang, Shilin Zhao, Haichun Yang, Bennett A Landman, and Yuankai Huo. Survival prediction of brain cancer with incomplete radiology, pathology, genomic, and demographic data. In *International Conference on Medical Image Computing and Computer-Assisted Intervention*, pages 626–635. Springer, 2022.
- Can Cui, Ruining Deng, Junchao Guo, Quan Liu, Tianyuan Yao, Haichun Yang, and Yuankai Huo. Enhancing physician flexibility: Prompt-guided multi-class pathological segmentation for diverse outcomes. In *2024 IEEE EMBS International Conference on Biomedical and Health Informatics (BHI)*, pages 1–8. IEEE, 2024.
- Ruining Deng, Can Cui, Lucas W Remedios, Shunxing Bao, R Michael Womick, Sophie Chiron, Jia Li, Joseph T

- Roland, Ken S Lau, Qi Liu, et al. Cross-scale attention guided multi-instance learning for crohn's disease diagnosis with pathological images. In *International Workshop on Multiscale Multimodal Medical Imaging*, pages 24–33. Springer, 2022.
- Alexey Dosovitskiy, Lucas Beyer, Alexander Kolesnikov, Dirk Weissenborn, Xiaohua Zhai, Thomas Unterthiner, Mostafa Dehghani, Matthias Minderer, Georg Heigold, Sylvain Gelly, et al. An image is worth 16x16 words: Transformers for image recognition at scale. *arXiv preprint arXiv:2010.11929*, 2020.
- Savannah R Duenweg, Samuel A Bobholz, Allison K Lowman, Margaret A Stebbins, Aleksandra Winiarz, Biprojit Nath, Fitzgerald Kyereme, Kenneth A Iczkowski, and Peter S LaViolette. Whole slide imaging (wsi) scanner differences influence optical and computed properties of digitized prostate cancer histology. *Journal of pathology informatics*, 14:100321, 2023.
- Chunyu Feng and Fei Liu. Artificial intelligence in renal pathology: current status and future. *Biomolecules and Biomedicine*, 23(2):225, 2023.
- Peng Gao, Shijie Geng, Renrui Zhang, Teli Ma, Rongyao Fang, Yongfeng Zhang, Hongsheng Li, and Yu Qiao. Clip-adapter: Better vision-language models with feature adapters. *International Journal of Computer Vision*, 132(2):581–595, 2024.
- Zhenhao Guo, Dingcheng Duan, Youwei Liang, Atharvraj Patil, and Pengtao Xie. Metabolitechat: A unified multimodal large language model for interactive metabolite analysis and functional insights. *bioRxiv*, pages 2025–11, 2025a.
- Zhenhao Guo, Rachit Saluja, Tianyuan Yao, Quan Liu, Yuankai Huo, Benjamin Liechty, David J Pisapia, Kenji Ikemura, Mert R Sabuncu, Yihe Yang, et al. Glo-vlms: Leveraging vision-language models for fine-grained diseased glomerulus classification. *arXiv preprint arXiv:2508.15960*, 2025b.
- Matthew G Hanna, Liron Pantanowitz, Rajesh Dash, James H Harrison, Mustafa Deebajah, Joshua Pantanowitz, and Hooman H Rashidi. Future of artificial intelligence (ai)-machine learning (ml) trends in pathology and medicine. *Modern Pathology*, page 100705, 2025.
- Kaiming He, Xiangyu Zhang, Shaoqing Ren, and Jian Sun. Deep residual learning for image recognition. In *Proceedings of the IEEE conference on computer vision and pattern recognition*, pages 770–778, 2016.
- Mohammad Reza Hosseinzadeh Taher, Fatemeh Haghghi, Ruibin Feng, Michael B Gotway, and Jianming Liang. A systematic benchmarking analysis of transfer learning for medical image analysis. In *MICCAI Workshop on Domain Adaptation and Representation Transfer*, pages 3–13. Springer, 2021.
- Edward J Hu, Yelong Shen, Phillip Wallis, Zeyuan Allen-Zhu, Yuanzhi Li, Shean Wang, Lu Wang, Weizhu Chen, et al. Lora: Low-rank adaptation of large language models. *ICLR*, 1(2):3, 2022.
- Zhi Huang, Federico Bianchi, Mert Yuksekgonul, Thomas J Montine, and James Zou. A visual–language foundation model for pathology image analysis using medical twitter. *Nature medicine*, 29(9):2307–2316, 2023.
- Sergey Ioffe and Christian Szegedy. Batch normalization: Accelerating deep network training by reducing internal covariate shift. In *International conference on machine learning*, pages 448–456. pmlr, 2015.
- Yihong Jin, Ze Yang, Juntian Liu, and Xinhe Xu. Anomaly detection and early warning mechanism for intelligent monitoring systems in multi-cloud environments based on llm. *arXiv preprint arXiv:2506.07407*, 2025.
- Adrienne Kline, Hanyin Wang, Yikuan Li, Saya Dennis, Meghan Hutch, Zhenxing Xu, Fei Wang, Feixiong Cheng, and Yuan Luo. Multimodal machine learning in precision health: A scoping review. *NPJ digital medicine*, 5(1): 171, 2022.
- Qunjuan Lei, Xiaoshuai Hou, Xumeng Liu, Dongmei Liang, Yun Fan, Feng Xu, Shaoshan Liang, Dandan Liang, Jing Yang, Guotong Xie, et al. Artificial intelligence assists identification and pathologic classification of glomerular lesions in patients with diabetic nephropathy. *Journal of Translational Medicine*, 22(1):397, 2024.
- Dong Li, Guihong Wan, Xintao Wu, Xinyu Wu, Ajit J Nirmal, Christine G Lian, Peter K Sorger, Yevgeniy R Semenov, and Chen Zhao. A survey on computational pathology foundation models: Datasets, adaptation strategies, and evaluation tasks. *arXiv preprint arXiv:2501.15724*, 2025a.
- Songtao Li and Hao Tang. Multimodal alignment and fusion: A survey. *arXiv preprint arXiv:2411.17040*, 2024.
- Xinyu Li, Can Cui, Ruining Deng, Yuxuan Tang, Quan Liu, Tianyuan Yao, and Yuankai Huo. Fine-grained multiclass nuclei segmentation with molecular empowered all-in-sam model. *Journal of Medical Imaging*, 12(5):057501–057501, 2025b.

- Fang Lu, Shan Hou, Chang Liu, Qing Li, Lin Wu, Ying Pan, Yangfan Wu, Hua Shu, Bo Zhang, Huijuan Mao, et al. Clinical significance of focal segmental glomerulosclerosis subclassification in iga nephropathy. *Nephrology Dialysis Transplantation*, page gfaf162, 2025.
- Ming Y Lu, Bowen Chen, Drew FK Williamson, Richard J Chen, Ivy Liang, Tong Ding, Guillaume Jaume, Igor Odintsov, Long Phi Le, Georg Gerber, et al. A visual-language foundation model for computational pathology. *Nature medicine*, 30(3):863–874, 2024.
- Yuzhe Lu, Haichun Yang, Zheyu Zhu, Ruining Deng, Agnes B Fogo, and Yuankai Huo. Improve global glomerulosclerosis classification with imbalanced data using circlemix augmentation. *arXiv preprint arXiv:2101.07654*, 2021.
- Anant Madabhushi and George Lee. Image analysis and machine learning in digital pathology: Challenges and opportunities. *Medical image analysis*, 33:170–175, 2016.
- Mieko Ochi, Daisuke Komura, and Shumpei Ishikawa. Pathology foundation models. *JMA journal*, 8(1):121–130, 2025.
- A Working Group of the International, IgA Nephropathy Network, Daniel C Cattran, Rosanna Coppo, H Terence Cook, John Feehally, Ian SD Roberts, Stéphan Troyanov, Charles E Alpers, Alessandro Amore, et al. The oxford classification of iga nephropathy: rationale, clinicopathological correlations, and classification. *Kidney international*, 76(5):534–545, 2009.
- Eva Pachetti and Sara Colantonio. A systematic review of few-shot learning in medical imaging. *Artificial intelligence in medicine*, 156:102949, 2024.
- Jonas Pfeiffer, Ivan Vulić, Iryna Gurevych, and Sebastian Ruder. Mad-x: An adapter-based framework for multi-task cross-lingual transfer. *arXiv preprint arXiv:2005.00052*, 2020.
- Alec Radford, Jong Wook Kim, Chris Hallacy, Aditya Ramesh, Gabriel Goh, Sandhini Agarwal, Girish Sastry, Amanda Askell, Pamela Mishkin, Jack Clark, et al. Learning transferable visual models from natural language supervision. In *International conference on machine learning*, pages 8748–8763. PmLR, 2021.
- M Rafieian-Kopaei, A Baradaran, and H Nasri. Significance of extracapillary proliferation in iga-nephropathy patients with regard to clinical and histopathological variables. *Hippokratia*, 17(3):258, 2013.
- Christopher J Roth, David A Clunie, David J Vining, Seth J Berkowitz, Alejandro Berlin, Jean-Pierre Bissonnette, Shawn D Clark, Toby C Cornish, Monief Eid, Cree M Gaskin, et al. Multispecialty enterprise imaging workgroup consensus on interactive multimedia reporting current state and road to the future: Himss-siim collaborative white paper. *Journal of digital imaging*, 34(3):495–522, 2021.
- Peter Schnuelle. Renal biopsy for diagnosis in kidney disease: indication, technique, and safety. *Journal of clinical medicine*, 12(19):6424, 2023.
- Sanjeev Sethi and Fernando C Fervenza. Standardized classification and reporting of glomerulonephritis. *Nephrology Dialysis Transplantation*, 34(2):193–199, 2019.
- Fereshteh Shakeri, Malik Boudiaf, Sina Mohammadi, Ivaxi Sheth, Mohammad Havaei, Ismail Ben Ayed, and Samira Ebrahimi Kahou. Fhist: a benchmark for few-shot classification of histological images. *arXiv preprint arXiv:2206.00092*, 2022.
- Jiangbo Shi, Zeyu Gao, Haichuan Zhang, Pargorn Puttapirat, Chunbao Wang, Xiangrong Zhang, and Chen Li. Effects of annotation granularity in deep learning models for histopathological images. In *2019 IEEE international conference on bioinformatics and biomedicine (BIBM)*, pages 2702–2708. IEEE, 2019.
- Benjamin D Simon, Kutsev Bengisu Ozyoruk, David G Gelikman, Stephanie A Harmon, and Barış Türkbey. The future of multimodal artificial intelligence models for integrating imaging and clinical metadata: a narrative review. *Diagnostic and Interventional Radiology*, 31(4):303, 2025.
- Krishna Prasad Varadarajan Srinivasan, Prasanth Gumpena, Madhusudhana Yattapu, and Vishal H Brahmbhatt. Comparative analysis of different efficient fine tuning methods of large language models (llms) in low-resource setting. *arXiv preprint arXiv:2405.13181*, 2024.
- Mohammad Reza Hosseinzadeh Taher, Fatemeh Haghghi, Michael B Gotway, and Jianming Liang. Large-scale benchmarking and boosting transfer learning for medical image analysis. *Medical image analysis*, 102:103487, 2025.
- Thijs W Cohen Tervaert, Antien L Mooyaart, Kerstin Amann, Arthur H Cohen, H Terence Cook, Cinthia B Drachenberg, Franco Ferrario, Agnes B Fogo, Mark Haas, Emile De Heer, et al. Pathologic classification of diabetic nephropathy. *Journal of the American Society of Nephrology*, 21(4):556–563, 2010.
- Tongzhou Wang and Phillip Isola. Understanding contrastive representation learning through alignment and

- uniformity on the hypersphere. In *International conference on machine learning*, pages 9929–9939. PMLR, 2020.
- Xiangxue Wang, Jingkai Zhang, Yuemei Xu, Yang Huang, Wenlong Ming, Yiping Jiao, Bicheng Liu, Xiangshan Fan, and Jun Xu. Glo-net: A dual task branch based neural network for multi-class glomeruli segmentation. *Computers in Biology and Medicine*, 186:109670, 2025. ISSN 0010-4825. . URL <https://www.sciencedirect.com/science/article/pii/S0010482525000204>.
- Cleo-Aron Weis, Jan Niklas Bindzus, Jonas Voigt, Marlen Runz, Svetlana Hertjens, Matthias M Gaida, Zoran V Popovic, and Stefan Porubsky. Assessment of glomerular morphological patterns by deep learning algorithms. *Journal of Nephrology*, 35(2):417–427, 2022.
- Parker C Wilson and Nidia Messias. How whole slide imaging and machine learning can partner with renal pathology, 2022.
- Xinhe Xu, Zhuoer Wang, Yihan Zhang, Yizhou Liu, Zhaoyue Wang, Zhihao Xu, Muhan Zhao, and Huaiying Luo. Style transfer: From stitching to neural networks. In *2024 5th International Conference on Big Data & Artificial Intelligence & Software Engineering (ICBASE)*, pages 526–530. IEEE, 2024.
- Tianyuan Yao, Yuzhe Lu, Ruining Deng, Zheyu Zhu, Zuhayr Asad, Haichun Yang, Lee E Wheless, Agnes B Fogo, and Yuankai Huo. Self-supervised learning with large-scale web image mining for characterizing glomerular lesions. In *Medical Imaging 2022: Digital and Computational Pathology*, volume 12039, pages 160–166. SPIE, 2022.
- Jiahui Yu, Zirui Wang, Vijay Vasudevan, Legg Yeung, Mojtaba Seyedhosseini, and Yonghui Wu. Coca: Contrastive captioners are image-text foundation models. *arXiv preprint arXiv:2205.01917*, 2022.
- Lining Yu, Mengmeng Yin, Ruining Deng, Quan Liu, Tianyuan Yao, Can Cui, Junlin Guo, Yu Wang, Yao-hong Wang, Shilin Zhao, et al. Glo-in-one-v2: holistic identification of glomerular cells, tissues, and lesions in human and mouse histopathology. *Journal of Medical Imaging*, 12(6):061406–061406, 2025.
- Sunyi Zheng, Xiaonan Cui, Yuxuan Sun, Jingxiong Li, Honglin Li, Yunlong Zhang, Pingyi Chen, Xueping Jing, Zhaoxiang Ye, and Lin Yang. Benchmarking pathclip for pathology image analysis. *Journal of Imaging Informatics in Medicine*, 38(1):422–438, 2025.